

A 2D covalent organic framework with ultra-large interlayer distance as high-rate anode material for lithium-ion batteries

Manman Wu^{1,2,3}, Yang Zhao^{1,3}, Hongtao Zhang^{1,3}, Jie Zhu^{1,3}, Yanfeng Ma^{1,3}, Chenxi Li^{1,3}, Yamin Zhang⁴, and Yongsheng Chen^{1,3} (✉)

¹ The Centre of Nanoscale Science and Technology and Key Laboratory of Functional Polymer Materials, Institute of Polymer Chemistry, College of Chemistry, Nankai University, Tianjin 300071, China

² State Key Laboratory of Elemento-Organic Chemistry, Nankai University, Tianjin 300071, China

³ Renewable Energy Conversion and Storage Center (RECAST), Nankai University, Tianjin 300071, China

⁴ State Key Laboratory of Applied Organic Chemistry, College of Chemistry and Chemical Engineering, Lanzhou University, Lanzhou 730000, China

© Tsinghua University Press and Springer-Verlag GmbH Germany, part of Springer Nature 2021

Received: 7 September 2021 / Revised: 18 October 2021 / Accepted: 23 October 2021

ABSTRACT

Covalent organic frameworks (COFs) have been broadly investigated for energy storage systems. However, many COF-based anode materials suffer from low utilization of redox-active sites and sluggish ions/electrons transport caused by their densely stacked layers. Thus, it is still a great challenge to obtain COF-based anode materials with fast ions/electrons transport and thus superior rate performance. Herein, a redox-active piperazine-terephthalaldehyde (PA-TA) COF with ultra-large interlayer distance is designed and synthesized for high-rate anode material, which contains piperazine units adopting a chair-shaped conformation with the nonplanar linkages of a tetrahedral configuration. This unique structure renders PA-TA COF an ultra-large interlayer distance of 6.2 Å, and further enables it to achieve outstanding rate and cycling performance. With a high specific capacity of 543 mAh·g⁻¹ even after 400 cycles at 1.0 A·g⁻¹, it still could afford a specific capacity of 207 mAh·g⁻¹ even at a high current density of 5.0 A·g⁻¹. Our study indicates that expanding the interlayer distance of COFs by rational molecular design would be of great importance to develop high-rate electrode materials for lithium-ion batteries.

KEYWORDS

lithium-ion batteries, high-rate anode material, covalent organic frameworks, ultra-large interlayer distance

1 Introduction

The rapidly and globally increasing demands of energy and the depletion of fossil fuels have raised concerns about the next-generation lithium-ion batteries (LIBs). Over the past decades, considerable efforts have been made to optimize the properties of electrode materials for LIBs [1, 2]. Nevertheless, how to obtain high performance electrode materials that can address the energy requirements in the future remains a great challenge. For example, graphite, as a mature anode material in current commercial LIBs, delivers a theoretical specific capacity of 372 mAh·g⁻¹ based on the reversible Li intercalation and the formation of LiC₆, and it still faces great challenges in many applications including large-scale electric vehicles [3]. To overcome capacity limitations, some high-capacity anode materials based on conversion or alloying reaction are developed such as Si, pure metals, alloys, metal oxides, or sulfides, the theoretical capacities of which are far beyond the capacity of graphite [2, 4]. However, the practical electrochemical performance of these anode materials is still limited by the huge volume expansion during the repeated cycling process [4–6]. Thus, it is a crucial issue to develop alternative anode materials with high capacity and outstanding cycling and rate performance for further development of LIBs.

Organic electrode materials can be promising alternatives for

LIBs with the advantages of abundant resource, low-cost, and structural diversity [7–10]. Moreover, many previous studies on organic anode materials have demonstrated that each C₆ aromatic ring can reversibly accept 6 Li⁺ to form a Li₆/C₆ complex instead of traditional Li/C₆, (e.g., naphthalene-1,4,5,8-tetracarboxylic dianhydride (NTCDA) and perylenetetracarboxylic dianhydride (PTCDA)), affording an incredible high theoretical capacity up to 2,200 mAh·g⁻¹ for each carbon atom [11–14]. Significantly, two-dimensional (2D) covalent organic frameworks (COFs) have emerged as newly organic materials for Li storage due to their structural features [15–20]. The stable framework structure of COFs can endow them good cycling stability [21–24]. Furthermore, when used as anode materials for LIBs, the containing π -conjugated aromatic rings in the structure of COFs can be utilized as redox-active moiety and undergo a multiple-electrons redox reaction, thus many COF-based anode materials are capable of affording high theoretical capacities [16–18].

However, the Li storage performance of many developed COFs-based anode materials is still unable to meet the demands for high-performance LIBs [14, 16, 17]. Generally, most traditional 2D COFs are constructed by aromatic backbones and planar linkages, resulting in strong interlayer π - π interactions, thus the 2D layers of COFs tend to stack densely in a parallel manner [17, 25]. As a result, a large number of interior redox-active sites in COFs are

Address correspondence to yschen99@nankai.edu.cn

deeply buried and unavailable for Li storage, which reduces the reversible practical capacity. Moreover, the closely stacked layers of COFs usually lead to sluggish ions diffusion, thus resulting in poor rate performance for LIBs [26, 27]. Therefore, to achieve high electrochemical performance, it is necessary to expand the interlayer distance of COFs and make full utilization of all the redox-active sites. Significantly, previous studies have indicated that both the building units and linkages of COFs have a significant influence on their interlayer spacing [28, 29]. Therefore, by taking advantages of the diversity of building units and linking groups for COFs, it is possible to obtain desired COFs with a large interlayer distance for high-performance anode materials.

With this, an aminor-linked piperazine-terephthalaldehyde (PA-TA) COF featured with ultra-large interlayer distance was designed and synthesized (Fig. 1). When adopted as anode material for LIBs, a large number of redox-active benzene rings in the structure of PA-TA COF can afford a high theoretical capacity. More importantly, the piperazine units and the nonplanar linking groups in PA-TA COF synergistically render it an ultra-large interlayer distance of 6.2 Å, far beyond that of traditional 2D COFs with planar linkages. Compared to previous reported anode materials with narrow interlayer spacing, the ultra-large interlayer spacing of PA-TA COF is beneficial to expose more redox-active sites and further facilitates the transport of ions, resulting in an

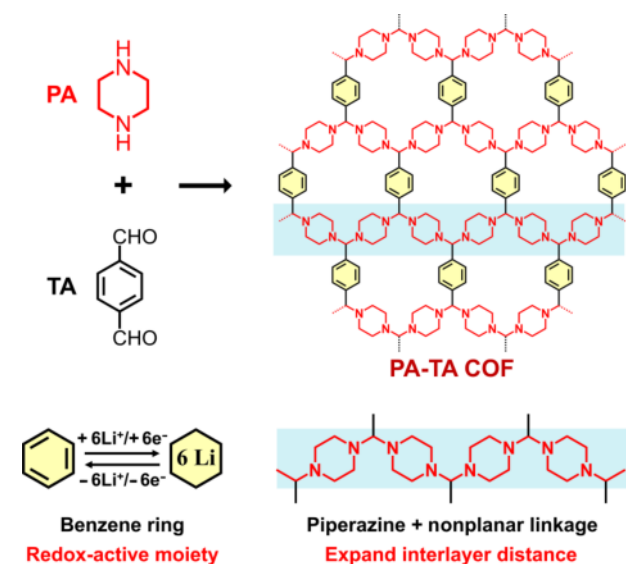


Figure 1 Schematic of the synthesis of PA-TA COF and the role of each component in PA-TA COF.

improved rate performance for LIBs. Benefiting from the above advantages, PA-TA COF delivers a high capacity of 543 mAh·g⁻¹ after 400 cycles at 1.0 A·g⁻¹, and affords a specific capacity of 207 mAh·g⁻¹ even at a high current density of 5.0 A·g⁻¹, showing both excellent cycling stability and rate performance.

2 Results and discussion

As shown in Fig. 1, PA-TA COF was designed and synthesized by the polycondensation of PA with TA. More detailed prepared process was given in the Experimental Section in the Electronic Supplementary Material (ESM). Notably, the as-designed PA-TA COF is composed of benzene rings, piperazine units, and aminor linkages. Among them, the benzene rings in PA-TA COF can serve as redox-active moiety and each C₆ aromatic ring can reversibly accept 6 Li⁺ to form a Li₆/C₆ complex in theory, thus endowing PA-TA COF a theoretical capacity as high as 596 mAh·g⁻¹. Furthermore, the piperazine units and the nonplanar linkages in PA-TA COF are contributed to reduce the aromatic stacking, which can efficiently expand the distance between layers of PA-TA COF. Therefore, when used as anode material for LIBs, the synergistic effect of the combination of these three components in PA-TA COF makes it capable of achieving superior rate performance with high capacity.

Fourier transform infrared spectroscopy (FTIR) was first performed to analyze the chemical composition of the as-obtained material. As shown in Fig. 2(a), the characteristic N–H stretching bands (3,246 cm⁻¹) disappear and the peak ascribed to aldehyde groups (1,692 cm⁻¹) diminishes, while the clear absorption at 1,330 cm⁻¹ can be observed in the FTIR spectrum of PA-TA COF, indicating the formation of aminor (N–C–N) linkages in the structure of PA-TA COF [28]. The ¹³C solid-state nuclear magnetic resonance (NMR) spectrum (Fig. 2(b)) further confirms the existence of N–C–N groups, where the resonance signal emerges at around 88.8 ppm, can be assigned to the carbon atoms located at N–C–N moieties [28]. Besides, the X-ray photoelectron spectroscopy (XPS) survey and high-resolution N 1s XPS spectrum (Fig. S1 in the ESM) of PA-TA COF also reveal its chemical composition. Elemental analysis results (Table S1 in the ESM) show a negligible deviation from the ideal C, H, and N values calculated by the repeating units of PA-TA COF. Thermal gravimetric analyses (TGA) curve (Fig. S2 in the ESM) of PA-TA COF shows good thermal stability up to ~ 290 °C under N₂ atmosphere, with less than 10% weight loss. In addition, N₂ adsorption–desorption isotherms at 77 K (Fig. 2(c)) display typical type I sorption isotherm profiles, suggesting the microporous

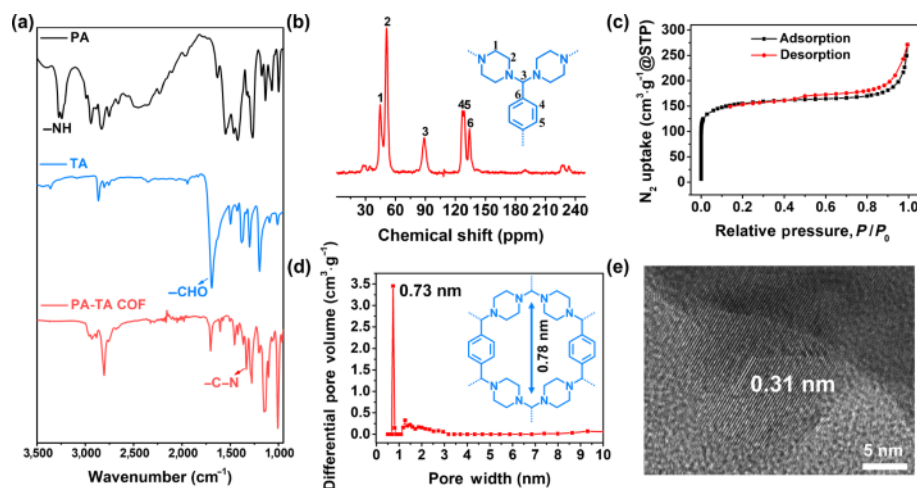


Figure 2 (a) FTIR spectra of PA, TA, and PA-TA COF. (b) ¹³C solid-state NMR spectrum of PA-TA COF. (c) N₂ adsorption–desorption isotherms and (d) pore-size distribution profile of PA-TA COF. (e) HRTEM image of PA-TA COF, showing clear lattice fringes with *d* spacing of 0.31 nm.

character of PA-TA COF [30]. The pore size of PA-TA COF (Fig. 2(d)) is calculated to be ~ 0.73 nm by using the nonlocal density functional theory method, which is close to the predicted pore size (~ 0.78 nm) according to the structure of PA-TA COF, indicating the formation of the well-defined channels in the structure of PA-TA COF. Furthermore, high-resolution transmission electron microscopy (HRTEM) image reveals a good crystallinity of PA-TA COF, as demonstrated by the clear lattice fringes in Fig. 2(e). The corresponding lattice spacing is measured to be 0.31 nm, which can be assigned to the (002) crystal plane of PA-TA COF.

Powder X-ray diffraction (PXRD) pattern of PA-TA COF also demonstrates its good crystallinity. The experimental PXRD pattern of PA-TA COF (Fig. 3(a), black curve) exhibits three sharp peaks at 11.14° , 14.74° , and 16.22° , which corresponds to the (100), (110), and (010) facets, respectively. Furthermore, the computational structural simulation and Pawley refined were performed to identify the crystal structure of PA-TA COF. As shown in Fig. 3(a), the experimental PXRD pattern is in good agreement with the simulated XRD pattern (blue curve) derived from the slipped AA stacking model of PA-TA COF. The Pawley refinement profile (grey curve) is well consistent with the experimentally observed pattern, as indicated by their negligible difference and very low R_{wp} and R_p values of 2.799% and 2.187%. Moreover, it is worth noting that the piperazine unit (purple circle in Fig. 3(b)) in PA-TA COF adopts a chair-shaped conformation, and the aminal linkage (green circle in Fig. 3(b)) has a tetrahedral configuration. These structural features render PA-TA COF an ultra-large interlayer distance of 6.2 Å (Fig. 3(c)), which is far larger than that of most 2D COFs with planar sp^2 linkages in previous reports. [28]. Different from the traditional 2D COFs with narrow interlayer spacing, PA-TA COF is able to improve the utilization of redox-active sites, and is beneficial to the insertion/extraction of Li^+ , which can afford it enhanced capacity and rate performance.

The potential application of PA-TA COF was evaluated as anode material for LIBs using coin type cells assembled with metal lithium as the counter/reference electrode. The typical cyclic voltammogram (CV) of PA-TA COF was performed in the potential window of 0.01–3.0 V with a $0.5 \text{ mV}\cdot\text{s}^{-1}$ sweep rate. As shown in Fig. 4(a), during the cathodic scan in the first cycle, the CV curve displays a prominent reduction peak at 0.58 V vs. Li/Li^+ , which can be ascribed to the formation of solid electrolyte

interphase (SEI) and the decomposition of electrolyte [16]. In the anodic process, the CV curve shows three anodic peaks at 0.25, 1.20, and 2.50 V, respectively, which suggests a multiple electron redox reaction of PA-TA COF. In the subsequent three cycles, the cathodic peak at 0.58 V disappears and the CV profiles overlap well, indicating the high redox reversibility of PA-TA COF as anode materials for LIBs.

The galvanostatic discharge curves are well consistent with the CV curves. As can be seen from Fig. 4(b), in the first discharge cycle, PA-TA COF delivers an ultrahigh initial capacity of $1,640 \text{ mAh}\cdot\text{g}^{-1}$ at a current density of $250 \text{ mA}\cdot\text{g}^{-1}$, which is mainly ascribed to the electrolyte decomposition and the SEI film formation widely observed for organic anode materials [16, 17]. Besides, the first discharge process displays a wide and stable voltage plateau at ~ 0.62 V, which is in good agreement with the reduction peak at 0.58 V in the CV curve. In the 2nd cycle, the capacity comes to the normal expected value of $556 \text{ mAh}\cdot\text{g}^{-1}$ with the disappearance of the false capacity caused by the SEI in the first cycle. Note, after 300 cycles, the discharge capacity of PA-TA COF increases to $633 \text{ mAh}\cdot\text{g}^{-1}$, and there is almost no capacity fading during the following cycles. After 450 cycles, a high reversible capacity of $637 \text{ mAh}\cdot\text{g}^{-1}$ with a high Coulombic efficiency of 99% is obtained (Fig. S3 in the ESM). The capacity of the conducting additive Ketjen black at various current densities is shown in Fig. S4 in the ESM, and the capacity contributions of Ketjen black in the electrode are 164 and $76 \text{ mAh}\cdot\text{g}^{-1}$ at 1.0 and $5.0 \text{ A}\cdot\text{g}^{-1}$, respectively. In addition, the phenomenon of capacity increase can be explained by the better electrolyte infiltration and improved Li^+ diffusion kinetics during cycling process [16].

The rate capabilities of PA-TA COF were also systematically investigated by discharge/charge cycling for 5 cycles at various current densities. As shown in Fig. 4(c), even at a high current density of $5.0 \text{ A}\cdot\text{g}^{-1}$, PA-TA COF still affords a high discharge capacity of $207 \text{ mAh}\cdot\text{g}^{-1}$, suggesting its excellent rate performance for LIBs. When the current density goes back to $0.5 \text{ A}\cdot\text{g}^{-1}$, PA-TA COF recovers a reversible capacity of $350 \text{ mAh}\cdot\text{g}^{-1}$, demonstrating its outstanding electrochemical stability under high current densities. Electrochemical impedance spectroscopy (EIS) was measured to investigate the reaction kinetics of PA-TA COF. As indicated in Fig. 4(d), the charge-transfer resistance (R_{ct}) of as-prepared half-cell is as low as 48.85Ω , suggesting a fast reaction kinetic of PA-TA COF as anode material for LIBs [19]. The superior rate performance of PA-TA COF is believed mainly due

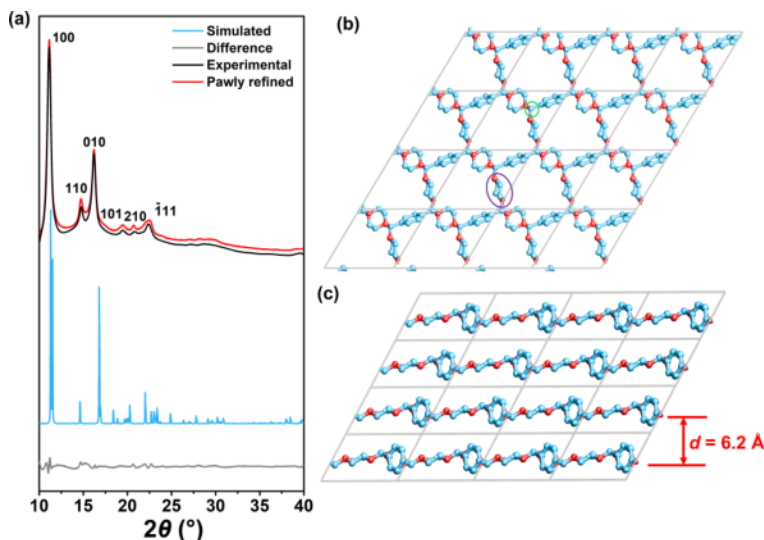


Figure 3 (a) XRD patterns of the experimentally observed (black), Pawley refined result (red), and their difference curve (gray), and simulated pattern with the slipped AA stacking (blue). (b) The simulated single layer crystal structure of PA-TA COF. (c) The side view of the slipped AA stacking mode, and the interlayer distance is 6.2 Å.

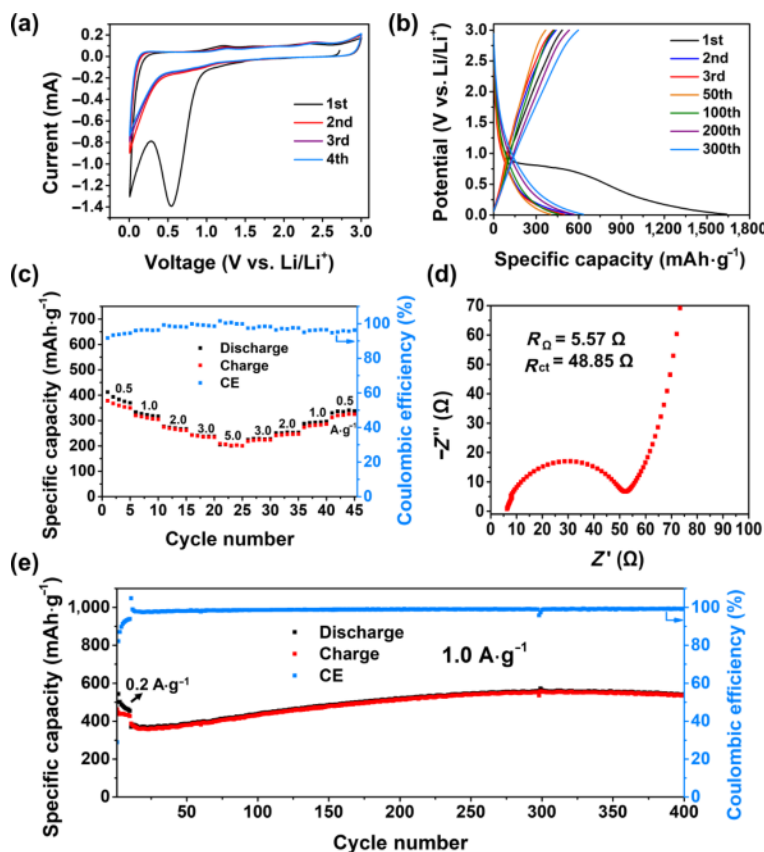


Figure 4 (a) The initial four-cycle cyclic voltammety curves of PA-TA COF at a scan rate of $0.5 \text{ mV}\cdot\text{s}^{-1}$. (b) The capacity–voltage profiles of PA-TA COF at a current density of $250 \text{ mA}\cdot\text{g}^{-1}$. (c) Rate capabilities of PA-TA COF at various current densities. (d) Electrochemical impedance spectrum of PA-TA COF. (e) Cycling performance of PA-TA COF at $1.0 \text{ A}\cdot\text{g}^{-1}$ for 400 cycles.

to its unique molecular structure with ultra-large interlayer spacing. Compared to commercial graphite and typical 2D COF anode materials with dense aromatic stacking, the ultra-large interlayer distance of PA-TA COF can efficiently facilitate the insertion/extraction of Li^+ with rapid transport kinetics, thus resulting in an elevated rate capacity. Besides, the well-defined channel structure of PA-TA COF is also conducive to the diffusion of ions and electrons, further improving the rate performance.

Furthermore, the cycling stability of PA-TA COF was evaluated at a high current density of $1.0 \text{ A}\cdot\text{g}^{-1}$. As shown in Fig. 4(e), after a small capacity decrease in the initial cycles, the obvious capacity increase can be observed and a high capacity of $543 \text{ mAh}\cdot\text{g}^{-1}$ after 400 cycles is obtained, exhibiting a high cycling stability. In addition, the stable framework of PA-TA COF also endows a good cycling performance. Moreover, the enlarged interlayer distance provides more interspace for volume changes resulting from the reversible cycling process, which efficiently avoids the structural collapse caused by a large number of Li^+ insertion/extraction, thus contributing to its excellent long-term cycling performance. The above outstanding electrochemical performance of PA-TA COF sufficiently confirms that expanding the interlayer spacing is an effective strategy to obtain high-performance anode materials with ultrahigh capacity, excellent rate, and cycling performance together. To further explore the potential of the PA-TA COF anode in a practical battery system, full cell was assembled by pairing LiFePO_4 (LFP) as the cathode. As shown in Fig. S5 in the ESM, the full cell shows reversible charging–discharging curves at an output voltage of 2.4 V and the active part of the anode delivers an energy density of ca. $216 \text{ Wh}\cdot\text{kg}^{-1}$, indicating that PA-TA COF anode can be regarded as a promising candidate for next-generation energy storage.

Furthermore, to gain deep insight into the fast rate capability of

PA-TA COF, CV measurements were performed to analyze its electrochemical reaction kinetics. As shown in Fig. 5(a), the CV curves are recorded from 0.01 to 3.0 V at various scan rates from 0.2 to $1.0 \text{ mV}\cdot\text{s}^{-1}$. Generally, the measured currents (i) at different scan rates obey a power law relationship with scan rates (ν): $i = a\nu^b$. The b value of 0.5 indicates a redox reaction limited by semi-infinite linear diffusion, while the b value closed to 1 implies a surface capacitive-controlled process [31–33]. Based on the above equation, the b value can be determined by the slope of the $\log(i) - \log(\nu)$ plots. As shown in Fig. 5(b), the corresponding slope values for the cathodic peak of PA-TA COF at different oxidation states are calculated to be 0.753 and 0.754 , respectively. The slope values indicate that the charge storage in PA-TA COF is a mixed process involving both the diffusive and capacitive processes, and is mainly dominated by capacitive-controlled, which results from the high reactivity of redox-active sites in PA-TA COF [31, 34]. Furthermore, the diffusive and capacitive-controlled contributions to the whole capacity of PA-TA COF are quantified. In theory, the total current response (i) is contributed by capacitance effect ($k_1\nu$) and diffusion process ($k_2\nu^{1/2}$), as the following Eq. (1)

$$i = k_1\nu + k_2\nu^{1/2} \quad (1)$$

where k_1 and k_2 constants can be determined by plotting $i\nu^{-1/2}$ versus $\nu^{1/2}$ [35, 36]. As shown in Fig. 5(c), the capacitive contribution at a scan rate of $0.4 \text{ mV}\cdot\text{s}^{-1}$ is calculated to be 50.0% . As the scan rate increases, the percentage of the capacitive contribution is further enhanced to 63.5% at $1.0 \text{ mV}\cdot\text{s}^{-1}$ (Fig. 5(d)). The above results suggest that the capacitive-controlled process plays an important role in the Li storage process of PA-TA COF and can be attributed to the fast Li^+ intercalation into the large interlayer spacing, especially for high rates, which is responsible for the excellent rate performance of PA-TA COF as the anode material for LIBs [35].

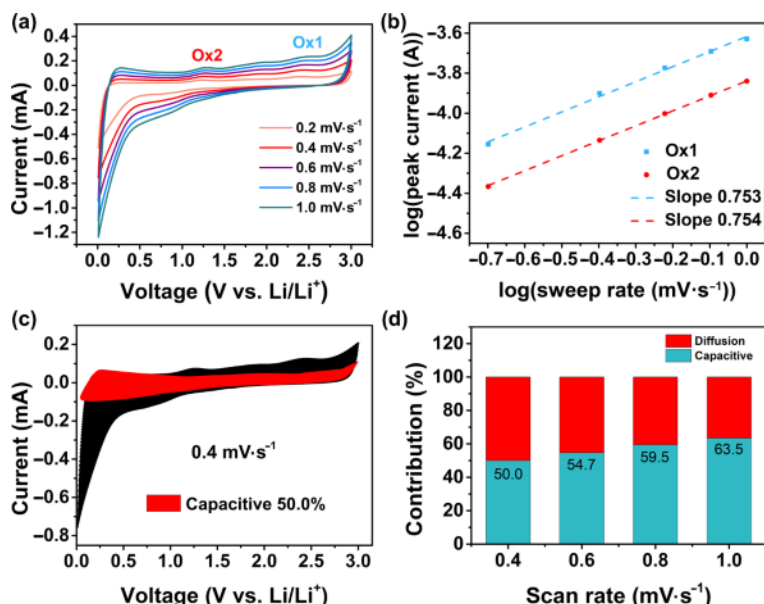


Figure 5 (a) The cyclic voltammograms at different sweep rates of PA-TA COF. (b) The plots of $\log(i)$ vs. $\log(v)$ to determine the b values of different peaks. (c) Capacitive contribution at $0.4 \text{ mV}\cdot\text{s}^{-1}$. (d) Separation of capacitive and diffusion currents at various scan rates.

3 Conclusions

In summary, by integrating piperazine and nonplanar linkage into the skeleton of COF, an aminated PA-TA COF featured with ultra-large interlayer distance was designed and synthesized as anode material for LIBs. It delivered a high capacity of $543 \text{ mAh}\cdot\text{g}^{-1}$ after 400 cycles at $1.0 \text{ A}\cdot\text{g}^{-1}$, and endowed a specific capacity of $207 \text{ mAh}\cdot\text{g}^{-1}$ even at a high current density of $5.0 \text{ A}\cdot\text{g}^{-1}$, showing both excellent cycling and rate performance. Besides, the electrochemical kinetic analysis revealed that the charge storage of PA-TA COF was mainly controlled by the capacitive process, contributing to fast reaction kinetics. Our results demonstrated that integrating nonplanar building units and linkages into 2D COFs to expand their interlayer spacing is of great significance for achieving high-performance anode materials for Li storage.

Acknowledgements

The authors gratefully acknowledge the financial support from Ministry of Science and Technology of China (No. 52090034), the National Natural Science Foundation of China (No. 51633002), and Higher Education Discipline Innovation Project (No. B12015).

Electronic Supplementary Material: Supplementary material (full details including reagents, the synthesis method of PA-TA COF, materials characterizations, electrochemical measurements, structure simulation, calculation of theoretical capacity, and additional table and figures) is available in the online version of this article at <https://doi.org/10.1007/s12274-021-3950-6>.

References

- [1] Li, M.; Lu, J.; Chen, Z. W.; Amine, K. 30 years of lithium-ion batteries. *Adv. Mater.* **2018**, *30*, 1800561.
- [2] Wu, F. X.; Maier, J.; Yu, Y. Guidelines and trends for next-generation rechargeable lithium and lithium-ion batteries. *Chem. Soc. Rev.* **2020**, *49*, 1569–1614.
- [3] Kim, H.; Choi, W.; Yoon, J.; Um, J. H.; Lee, W.; Kim, J.; Cabana, J.; Yoon, W. S. Exploring anomalous charge storage in anode materials for next-generation Li rechargeable batteries. *Chem. Rev.* **2020**, *120*, 6934–6976.
- [4] Lu, Y.; Zhang, Q.; Chen, J. Recent progress on lithium-ion batteries with high electrochemical performance. *Sci. China Chem.* **2019**, *62*, 533–548.
- [5] Zuo, X. X.; Zhu, J.; Müller-Buschbaum, P.; Cheng, Y. J. Silicon based lithium-ion battery anodes: A chronicle perspective review. *Nano Energy* **2017**, *31*, 113–143.
- [6] Aravindan, V.; Lee, Y. S.; Madhavi, S. Research progress on negative electrodes for practical Li-ion batteries: Beyond carbonaceous anodes. *Adv. Energy Mater.* **2015**, *5*, 1402225.
- [7] Lee, S.; Kwon, G.; Ku, K.; Yoon, K.; Jung, S. K.; Lim, H. D.; Kang, K. Recent progress in organic electrodes for Li and Na rechargeable batteries. *Adv. Mater.* **2018**, *30*, 1704682.
- [8] Schon, T. B.; McAllister, B. T.; Li, P. F.; Seferos, D. S. The rise of organic electrode materials for energy storage. *Chem. Soc. Rev.* **2016**, *45*, 6345–6404.
- [9] Muench, S.; Wild, A.; Friebe, C.; Häupler, B.; Janoschka, T.; Schubert, U. S. Polymer-based organic batteries. *Chem. Rev.* **2016**, *116*, 9438–9484.
- [10] Zhao, Y.; Wu, M. M.; Chen, H. B.; Zhu, J.; Liu, J.; Ye, Z. T.; Zhang, Y.; Zhang, H. T.; Ma, Y. F.; Li, C. X. et al. Balance cathode-active and anode-active groups in one conjugated polymer towards high-performance all-organic lithium-ion batteries. *Nano Energy* **2021**, *86*, 106055.
- [11] Wu, J. S.; Rui, X. H.; Wang, C. Y.; Pei, W. B.; Lau, R.; Yan, Q. Y.; Zhang, Q. C. Nanostructured conjugated ladder polymers for stable and fast lithium storage anodes with high capacity. *Adv. Energy Mater.* **2015**, *5*, 1402189.
- [12] Han, X. Y.; Qing, G. Y.; Sun, J. T.; Sun, T. L. How many lithium ions can be inserted onto fused C_6 aromatic ring systems? *Angew. Chem., Int. Ed.* **2012**, *51*, 5147–5151.
- [13] Wu, J. S.; Rui, X. H.; Long, G. K.; Chen, W. Q.; Yan, Q. Y.; Zhang, Q. C. Pushing up lithium storage through nanostructured polyazaacene analogues as anode. *Angew. Chem., Int. Ed.* **2015**, *54*, 7354–7358.
- [14] Lin, Z. Q.; Xie, J.; Zhang, B. W.; Li, J. W.; Weng, J. N.; Song, R. B.; Huang, X.; Zhang, H.; Li, H.; Liu, Y. et al. Solution-processed nitrogen-rich graphene-like holey conjugated polymer for efficient lithium ion storage. *Nano Energy* **2017**, *41*, 117–127.
- [15] Yao, C. J.; Wu, Z. Z.; Xie, J.; Yu, F.; Guo, W.; Xu, Z. J.; Li, D. S.; Zhang, S. Q.; Zhang, Q. C. Two-dimensional (2D) covalent organic framework as efficient cathode for binder-free lithium-ion battery. *ChemSusChem* **2020**, *13*, 2457–2463.
- [16] Lei, Z. D.; Chen, X. D.; Sun, W. W.; Zhang, Y.; Wang, Y. Exfoliated triazine-based covalent organic nanosheets with multielectron redox for high-performance lithium organic batteries. *Adv. Energy Mater.* **2019**, *9*, 1801010.
- [17] Chen, X. D.; Li, Y. S.; Wang, L.; Xu, Y.; Nie, A. M.; Li, Q. Q.; Wu,

- F.; Sun, W. W.; Zhang, X.; Vajtai, R. et al. High-lithium-affinity chemically exfoliated 2D covalent organic frameworks. *Adv. Mater.* **2019**, *31*, 1901640.
- [18] Lei, Z. D.; Yang, Q. S.; Xu, Y.; Guo, S. Y.; Sun, W. W.; Liu, H.; Lv, L. P.; Zhang, Y.; Wang, Y. Boosting lithium storage in covalent organic framework via activation of 14-electron redox chemistry. *Nat. Commun.* **2018**, *9*, 576.
- [19] Wu, M. M.; Zhao, Y.; Sun, B. Q.; Sun, Z. H.; Li, C. X.; Han, Y.; Xu, L. Q.; Ge, Z.; Ren, Y. X.; Zhang, M. T. et al. A 2D covalent organic framework as a high-performance cathode material for lithium-ion batteries. *Nano Energy* **2020**, *70*, 104498.
- [20] Xie, H. Y.; Hao, Q.; Jin, H. C.; Xie, S.; Sun, Z. W.; Ye, Y. D.; Zhang, C. H.; Wang, D.; Ji, H. X.; Wan, L. J. Redistribution of Li-ions using covalent organic frameworks towards dendrite-free lithium anodes: A mechanism based on a Galton board. *Sci. China Chem.* **2020**, *63*, 1306–1314.
- [21] Zhao, X. J.; Pachfule, P.; Thomas, A. Covalent organic frameworks (COFs) for electrochemical applications. *Chem. Soc. Rev.* **2021**, *50*, 6871–6913.
- [22] Kong, L. J.; Liu, M.; Huang, H.; Xu, Y. H.; Bu, X. H. Metal/covalent-organic framework based cathodes for metal-ion batteries. *Adv. Energy Mater.*, in press, DOI: 10.1002/aenm.202100172.
- [23] Zhou, L. M.; Jo, S.; Park, M.; Fang, L.; Zhang, K.; Fan, Y. P.; Hao, Z. M.; Kang, Y. M. Structural engineering of covalent organic frameworks for rechargeable batteries. *Adv. Energy Mater.* **2021**, *11*, 2003054.
- [24] Kandambeth, S.; Kale, V. S.; Shekhah, O.; Alshareef, H. N.; Eddaoudi, M. 2D covalent-organic framework electrodes for supercapacitors and rechargeable metal-ion batteries. *Adv. Energy Mater.*, in press, DOI: 10.1002/aenm.202100177.
- [25] Li, J.; Jing, X. C.; Li, Q. Q.; Li, S. W.; Gao, X.; Feng, X.; Wang, B. Bulk COFs and COF nanosheets for electrochemical energy storage and conversion. *Chem. Soc. Rev.* **2020**, *49*, 3565–3604.
- [26] Sun, T.; Xie, J.; Guo, W.; Li, D. S.; Zhang, Q. C. Covalent-organic frameworks: Advanced organic electrode materials for rechargeable batteries. *Adv. Energy Mater.* **2020**, *10*, 1904199.
- [27] Wang, S.; Wang, Q. Y.; Shao, P. P.; Han, Y. Z.; Gao, X.; Ma, L.; Yuan, S.; Ma, X. J.; Zhou, J. W.; Feng, X. et al. Exfoliation of covalent organic frameworks into few-layer redox-active nanosheets as cathode materials for lithium-ion batteries. *J. Am. Chem. Soc.* **2017**, *139*, 4258–4261.
- [28] Jiang, S. Y.; Gan, S. X.; Zhang, X.; Li, H.; Qi, Q. Y.; Cui, F. Z.; Lu, J.; Zhao, X. Amino-linked covalent organic frameworks through condensation of secondary amine with aldehyde. *J. Am. Chem. Soc.* **2019**, *141*, 14981–14986.
- [29] Peng, Y. W.; Huang, Y.; Zhu, Y. H.; Chen, B.; Wang, L. Y.; Lai, Z. C.; Zhang, Z. C.; Zhao, M. T.; Tan, C. L.; Yang, N. L. et al. Ultrathin two-dimensional covalent organic framework nanosheets: Preparation and application in highly sensitive and selective DNA detection. *J. Am. Chem. Soc.* **2017**, *139*, 8698–8704.
- [30] Xu, S. Q.; Wang, G.; Biswal, B. P.; Addicoat, M.; Paasch, S.; Sheng, W. B.; Zhuang, X. D.; Brunner, E.; Heine, T.; Berger, R. et al. A nitrogen-rich 2D sp²-carbon-linked conjugated polymer framework as a high-performance cathode for lithium-ion batteries. *Angew. Chem., Int. Ed.* **2019**, *58*, 849–853.
- [31] Zhao, G. F.; Zhang, Y. H.; Gao, Z. H.; Li, H. N.; Liu, S. M.; Cai, S.; Yang, X. F.; Guo, H.; Sun, X. L. Dual active site of the azo and carbonyl-modified covalent organic framework for high-performance Li storage. *ACS Energy Lett.* **2020**, *5*, 1022–1031.
- [32] Sun, R. M.; Hou, S.; Luo, C.; Ji, X.; Wang, L. N.; Mai, L. Q.; Wang, C. S. A covalent organic framework for fast-charge and durable rechargeable Mg storage. *Nano Lett.* **2020**, *20*, 3880–3888.
- [33] Wang, G.; Chandrasekhar, N.; Biswal, B. P.; Becker, D.; Paasch, S.; Brunner, E.; Addicoat, M.; Yu, M. H.; Berger, R.; Feng, X. L. A crystalline, 2D polyarylimide cathode for ultrastable and ultrafast Li storage. *Adv. Mater.* **2019**, *31*, 1901478.
- [34] Wang, Y. R.; Liu, Z. T.; Wang, C. X.; Hu, Y.; Lin, H. N.; Kong, W. H.; Ma, J.; Jin, Z. π -Conjugated polyimide-based organic cathodes with extremely-long cycling life for rechargeable magnesium batteries. *Energy Storage Mater.* **2020**, *26*, 494–502.
- [35] Wu, C. G.; Hu, M. J.; Yan, X. R.; Shan, G. C.; Liu, J. Z.; Yang, J. Azo-linked covalent triazine-based framework as organic cathodes for ultrastable capacitor-type lithium-ion batteries. *Energy Storage Mater.* **2021**, *36*, 347–354.
- [36] Han, C. P.; Tong, J.; Tang, X.; Zhou, D.; Duan, H.; Li, B. H.; Wang, G. X. Boost anion storage capacity using conductive polymer as a pseudocapacitive cathode for high-energy and flexible lithium ion capacitors. *ACS Appl. Mater. Interfaces* **2020**, *12*, 10479–10489.